SUPPLEMENTAL MATERIAL for:

Thin liquid film as an optical nonlinear-nonlocal media and memory element in integrated optofluidic reservoir computer

Chengkuan Gao, Prabhav Gaur, Shimon Rubin and Yeshaiahu Fainman

Department of Electrical and Computer Engineering, University of California, San Diego, 9500 Gilman Dr., La Jolla, California 92023, USA

S.1. GOVERNING EQUATIONS AND KEY PARAMETERS

Below we present the governing equations for the optical field, heat transport, fluid dynamics and the matching conditions across the gas-liquid interface. The coupling scheme between the four mechanisms operates as follows. First, the propagating optical WG mode interacts with the gold patch and induces heating which is triggers temperature gradient of the gas-liquid interface, leading in turn to gradients of the surface tension. The latter invokes TC flows and thickness changes of the liquid film, leading to changes of the effective refractive index of the optical mode.

S.1.1. Optical field

Faraday and Ampere's law equations relating between electrical field $\vec{E}$, magnetic field $\vec{B}$, electric displacement $\vec{D}$, magnetic induction $\vec{H}$ and current density $\vec{J}$ are given by

$$\vec{\nabla} \times \vec{E} = -\frac{\partial \vec{B}}{\partial t} \tag{S1a}$$

$$\vec{\nabla} \times \vec{H} = \frac{\partial \vec{D}}{\partial t} + \vec{J}. \tag{S1b}$$

Applying $\vec{\nabla} \times$ operator on Eq.S1a and then employing: constitutive relation $\vec{B} = \mu \vec{H}$, Eq.S1b and Joule's law $\vec{J} = \sigma \vec{E}$, yields

$$\vec{\nabla} \times \left(\frac{1}{\mu_r} \vec{\nabla} \times \vec{E} \right) = k_0^2 \left(\epsilon_r - \frac{i\sigma}{\omega \epsilon_0} \right) \vec{E}. \tag{S2}$$

Here, $k_0^2 = \omega^2 \epsilon_0$; ϵ_0 and μ_0 are electric and magnetic vacuum permittivities, respectively; ϵ_r and μ_r are electric permittivity and magnetic permittivity, respectively.

S.1.2. Heat transport

Heat diffusion transport is governed by the following diffusion equation for the temperature field T,

$$\rho_m c_p \frac{\partial T}{\partial t} - \vec{\nabla} \cdot \left(k_{th} \vec{\nabla} T \right) = \vec{J} \cdot \vec{E}, \tag{S3}$$

Where ρ_m, c_p, k_{th} are the corresponding material density, specific heat and heat conductivity, and the term $\vec{J} \cdot \vec{E}$ is the Joule heat source term.

S.1.3. Fluid dynamics of liquid and gas

Dynamics of a Newtonian, non-compressible fluid in cartesian coordinates is governed by the Navier-Stokes equations given by

$$\rho \left(\frac{\partial u_i}{\partial t} + u_j \frac{\partial}{\partial x^j} u_i \right) = \frac{\partial}{\partial x^j} \tau_{ij} + F_i; \quad i, j = x, y, z, \tag{S4}$$

where τ_{ij} is the corresponding energy-momentum tensor given by

$$\tau_{ij} = -p\delta_{ij} + \mu e_{ij}; \quad e_{ij} = \frac{\partial u_i}{\partial x_j} + \frac{\partial u_j}{\partial x_i} - \frac{2}{3}\delta_{ij}\frac{\partial u_l}{\partial x_l}. \tag{S5}$$

Here, u_i, F_i, ρ, p and μ are the fluid velocity components, body force components, density, pressure, and dynamic viscosity, respectively. The indices i, j run over the three Cartesian coordinates x, y, z, and summation convention over repeated indices is employed.

S.1.4. Gas-liquid matching conditions

The interfacial Stress Balance Equation (SBE) which holds on the gas-liquid (or liquid-liquid or gas-gas) interface, is given by the following matching conditions

$$\hat{n}_j \cdot \left[\tau_{ij}^{(2)} - \tau_{ij}^{(1)} \right] = \sigma \hat{n}_i \frac{\partial \hat{n}_j}{\partial x_j} - \frac{\partial \sigma}{\partial x_i}, \tag{S6}$$

which in vector notation takes the following form

$$\hat{n} \cdot \left(-pI + \mu \left(\vec{\nabla}\vec{u}^T + \vec{\nabla}\vec{u} - \frac{2}{3}\vec{\nabla} \cdot \vec{u} \right) \right) = \sigma \hat{n}(\vec{\nabla} \cdot \hat{n}) - \vec{\nabla}\sigma. \tag{S7}$$

Normal stress balance and tangential stress balance are obtained by projecting SBE on $\hat{n}$ and $\hat{t}$, respectively, and are given by

$$\hat{n} \cdot \left(-pI + \mu \left(\vec{\nabla}\vec{u}^T + \vec{\nabla}\vec{u} - \frac{2}{3}\vec{\nabla}\cdot\vec{u} \right) \right) \cdot \hat{n} = \sigma(\vec{\nabla}\cdot\hat{n}), \tag{S8a}$$

$$\hat{n} \cdot \left(-pI + \mu \left(\vec{\nabla}\vec{u}^T + \vec{\nabla}\vec{u} - \frac{2}{3}\vec{\nabla}\cdot\vec{u} \right) \right) \cdot \hat{t} = \sigma_T \nabla_t T, \tag{S8b}$$

where in the last line we used $\hat{t} \cdot \vec{\nabla}\sigma \equiv \nabla_t \sigma$ and assumed the commonly employed linear dependence of surface tension on temperature $\sigma(T) = \sigma_0 - \sigma_T T$ (σ_0 and σ_T are typically positive constants).

S.1.5. Boundary conditions

Heat transport: Dirichlet boundary conditions of fixed temperature 20° on the boundary.

Liquid: Navier boundary conditions on the vertical walls with built-in factor of minimum element length equal to one. On horizontal walls we employed vanishing slip velocity conditions.

Optical field: PML boundary conditions in order to reduce reflections from the boundaries.

S.1.6. Numerical values used

The table below specifies the numerical values employed in the multiphysics simulations. All parameters are at 293.15 K, 1 atm, and for wavelength 1550 nm.

Liquid's surface tension is assumed to depend linearly on the temperature, $\sigma(T) = \sigma_0 - \sigma_T(T - T_0)$, where T_0 is the ambient temperature, $\sigma_0 = 10^{-3}$ N/m, and $\sigma_T = 10^{-4}$ N/(m·K).

S.2. COMPARISON BETWEEN TC-BASED AND TO-BASED SELF-INDUCED PHASE CHANGE

To compare the self-induced phase change due to TC and TO effects, denoted by $\Delta\varphi_{TC}$ and $\Delta\varphi_{TO}$, respectively, we compare simulation results of a single active WG

	gas	liquid	Si	Si0$_2$	Gold	SiN
Thermal conductivity, k_{th} [W/(m·K)]	0.026	0.15	130	1.38	310	30
Density, ρ [kg/m^3]	1.2	930	2329	2203	19300	2500
Constant pressure heat capacity, c_p [J/(kg·K)]	1005.5	1500	700	703	125	170
complex refractive index, n + i·k	1	1.444	3.4757	1.444	0.52406 + 10.742·i	2
Dynamic viscosity, μ [Pa·s]	1.8·10^{-5}	0.1	-	-	-	-
Ratio of specific heats, c_p/c_V	1.4	1.5	-	-	-	-

TABLE S1. Key physical parameters employed in the multiphysics simulation.

described in Fig.2 to a similar simulation where the 500 nm thick liquid film is replaced by a solid film of identical thickness and refractive index, but which is not allowed to deform. Fig.S1 presents comparison between the self-induced phase change of the two cases indicating that the magnitude of the effect is of the order $\Delta\varphi_{TC}/\Delta\varphi_{TO} \sim 500 - 1000$ Furthermore, while the $\Delta\varphi_{TO}$ presents linear behavior in optical power, $\Delta\varphi_{TO}$ presents nonlinear behavior due to nonlinear relation and also to saturation due to depletion of the liquid above the gold patch.

S.3.   SELF-INDUCED REFLECTION

Fig.S2 presents 3D simulation results of the gas-liquid interface evolving geometry during the process of self-induced reflection, at time moments 0 ms, 10 ms, 20 ms. The transmittance during this process is described by the blue curve in Fig.4d, indicating lower transmittance values as liquid film above the Bragg WG becomes thinner. Similarly to the case of self-induced transmittance, Fig.4c presents the geometry of the Bragg WG designed to support the case of self-induced reflection with the following parameters: $a = 0.7$ μm, $b = 0.4$ μm, $c = 0.6$ μm, $d = 0.4$ μm, $k = 0.02$ μm, and gold patch on all 15 SiN ribs except the second and the fourth rib.
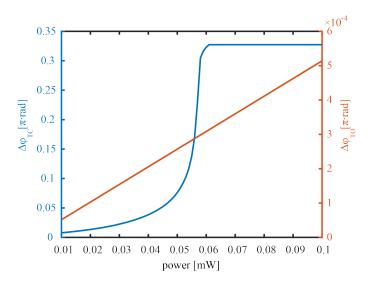
FIG. S1. Simulation results comparing the self-induced phase changes $\Delta\varphi_{TC}$ and $\Delta\varphi_{TO}$ under TC and TO effects, respectively. The result indicates that TC-driven mechanism is approximately three orders of magnitude larger compared to TO effect under similar optical powers. The value of TO coefficient of silicon employed in our simulation is $dn/dT = 1.8 \cdot 10^{-4}\,1/\mathrm{K}$ [43].

S.4. EVOLUTION OF DYNAMICAL PROCESS AS RNN AND PROOF OF EQ.3

First order partial differential equation governing evolution of physical observable A can be written as

$$\frac{\partial A(\vec{r},t)}{\partial t} + H\big[A(\vec{r},t),\vec{\nabla}A(\vec{r},t),t\big]A(\vec{r},P(t),t) = J(t), \tag{S9}$$

where H is a function which depends on A, its spatial derivatives $\vec{\nabla}A$, and time dependent coefficient $P(t)$; $J(t)$ is an additional source term. Introducing spatial discretization and grid points labelled by vectors α, β (e.g. $\alpha = (x_\alpha, y_\alpha, z_\alpha)$ is a position vector pointing to the relevant grid point in the 3D space), allows to rewrite Eq.S9 as the following system of first order ordinary differential equations

$$\frac{dA_\alpha(t)}{dt} + H_{\alpha\beta}\big[A_\gamma(t),P(t)\big]A_\beta(t) = J_\alpha(t), \tag{S10}$$

where $A_\alpha(t) \equiv A(\vec{r}_\alpha,t)$, $J_\alpha(t) \equiv J(\vec{r}_\alpha,t)$ and $H_{\alpha\beta} \equiv H(\vec{r}_\alpha,\vec{r}_\beta,t)$ are the values of the corresponding quantities sampled at the relevant spatial points, summation over repeated indices is assumed, and α runs over all grid points. Employing time discretization with small time step Δt (for the particular case of piece-wise constant

self-induced reflection
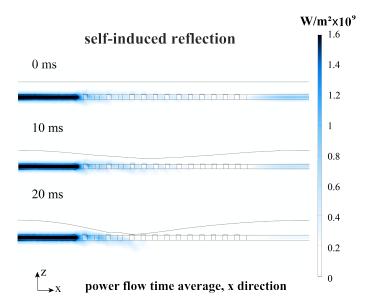
power flow time average, x direction

FIG. S2. Numerical results presenting the evolving geometry of the gas-liquid interface during the process of self-induced reflection, at time moments 0 ms, 10 ms, 20 ms, thus complementing the results presented in Fig.4.

excitation described in Fig.5 the time step coincides with $\tau_{W,r}$ which isn't necessarily small), allows to rewrite Eq.S10 as

$$A_\alpha(t) = A_\alpha(t - \Delta t) - \Delta t \cdot \left(H_{\alpha\beta} \big[A_\gamma(t), P(t) \big] A_\beta(t) + J_\alpha(t) \right), \tag{S11}$$

where we have used the Calculus theorem stating that if derivative exists then its left and right limits exist and are equal. Substituting the expression for $A_\alpha(t)$ given by Eq.S11 to express $A_\beta(t), A_\gamma(t)$ in the right hand side of Eq.S11, and furthermore keeping first order terms in Δt yields

$$A_\alpha(t) = f \big[A_\alpha(t - \Delta t), P(t) \big] \equiv$$
$$A_\alpha(t - \Delta t) - \Delta t \cdot \left(H_{\alpha\beta} \big[A_\gamma(t - \Delta t), P(t) \big] A_\beta(t - \Delta t) + J_\alpha(t) \right), \tag{S12}$$

which admits a functional form of RNN update equation similar to Eq.3. While Eq.S9 describes dynamics of various degrees of freedom such as heat transport, deformation of thin liquid films, mass transport and quantum wave-function, the approach above can be generalized to practically any system including those described by second order systems in time. For the particular case of thin liquid film of constant viscosity, vanishing body and surface forces, as well as vanishing slip velocity on the boundary, Eq.S9 takes the

form

$$\frac{\partial h}{\partial t} + \frac{1}{\mu}\vec{\nabla}_{\parallel} \cdot \left(\frac{1}{2}h^2\vec{\nabla}_{\parallel}\sigma + \frac{\sigma_0}{3}h^3\vec{\nabla}_{\parallel}\nabla_{\parallel}^2 h\right) = 0, \tag{S13}$$

which can be formally rewritten as Eq.S10

$$\frac{\partial h}{\partial t} + H(h)h = 0; \quad H(h) \equiv \frac{1}{\mu}\left(\frac{h}{2}\nabla_{\parallel}^2\sigma + \vec{\nabla}_{\parallel}h \cdot \vec{\nabla}_{\parallel}\sigma + \frac{\sigma_0 h^2}{3}\nabla_{\parallel}^4 h + \sigma_0 h\vec{\nabla}_{\parallel}h \cdot \vec{\nabla}_{\parallel}\nabla_{\parallel}^2 h\right). \tag{S14}$$

Consequnetly, following the same steps as above one can readily rewrite Eq.S14 as RNN update equation Eq.S12 (i.e. Eq.3 in the main text with different notation for the time argument).

S.5. CONSTRUCTING RC SIMULATION

To construct RC simulation we employed the following three steps: (i) collected dynamics of $h_c(t)$ as a function of time for numerous driving optical powers and initial conditions; (ii) constructed reduced 1D model describing dynamics of $h_c(t)$ under first order ordinary different equation with power dependent coefficients; (iii) employed the reduced evolution equation to simulate dynamics of thin liquid film under driving optical sequence, collect the corresponding output data and then perform reservoir training and test its performance.

S.5.1. Dynamics of $h_c(t)$ as a function of time for numerous driving optical powers and initial conditions

Fig.S3 presents evolution of $h_c(t)$ as a function of various optical power levels and several initial conditions which reflect the anticipated working regime. The optical power levels used to generate the curves described by Fig.S3a in the following ranges are: in range $0.01 - 0.03$ mW with alternating steps 0.003 mW and 0.002 mW; in range $0.031 - 0.07$ mW with constant step of 0.001 mW; in range $0.073 - 0.1$ mW with alternating steps 0.003 mW and 0.002 mW. For restoring curves presented in Fig.S3b we employed powers between $0.01 - 0.05$ mW with alternating steps of 0.003 and 0.002 mW. Importantly, to generate the curves we employed temperature equivalent optical power allowing to significantly reduce the computational cost of each model in terms of memory
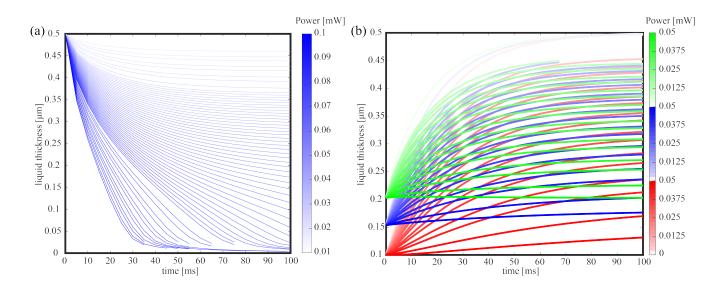
7

FIG. S3. Numerical results presenting thickness of thin liquid film of initial thickness $h_c(0) = 500$ nm at a central point above the gold patch as a function of time for various optical powers and various initial conditions. (a) Liquid film thickness as a function of time under approximately 65 different power levels in the range bracketed by 0.01 mW and 0.1 mW describing film thinning. (b) Liquid thickness $h_c(t)$ for initial conditions $0.1, 0.15, 0.2$ μm; each liquid thickness of corresponding to the initial conditions above is subject under approximately 15 different power levels in the range below 0.05 mW corresponding to film relaxation to thicker configuration.

and computation time at the cost of introducing a small error. Since under optical excitation the temperature reaches equilibrium on time scale of few milliseconds, which is sufficiently smaller compared to time scales governing evolution of thin liquid film, introducing equivalent temperature source won't affect significantly the liquid dynamics during the relevant time scale. Furthermore, since our RC simulation operates with liquid films of thickness above 100 nm, we expect that changes of the optical mode due to evolving liquid thickness, will not lead to significant changes of optical heat dissipation and temperature values. Fig.S4 summarizes some of the simplifying assumptions we employed during the construction of the reservoir simulation. Fig.S4a presents the mean steady state temperature (T) in the gold patch for 10 cases of different optical power level (P), and the corresponding linear fit which is explicitly given by

$$T = 15.75 \cdot P + 293.15. \tag{S15}$$

Fig.S4b presents three evolution curves of liquid thickness above the gold patch center,
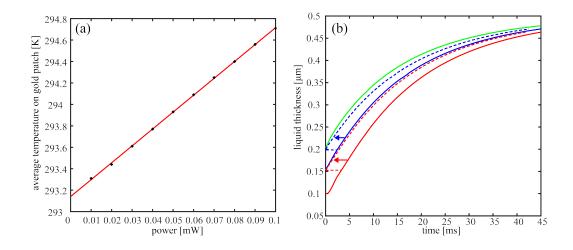
8

FIG. S4. Simulation results summarizing the simplifying assumption followed during the construction of RC simulation. (a) Linear relation between the optical power (P) in the WG to the mean temperature (T) in the gold patch on top of the WG enabling to replace the optical source by equivalent effective temperature boundary condition. (b) Comparison of relaxation dynamics under different initial conditions, enabling to implement a single model for all cases irrespective of previous history.

for three different initial conditions (0.1 μm, 0.15 μm, 0.2 μm) and compares the evolution of the 0.2 μm curve with 0.15 μm curve and the evolution of 0.15 μm curve with 0.1 μm curve. The comparison is achieved by translating the 0.1 μm and 0.15 μm curves to the initial values of 0.15 μm and 0.2 μm, respectively; the shifted curves are presented as dashed lines. The comparison indicates very small difference in liquid evolution.

S.5.2.   Reduced 1D model for $h_c(t)$ and phase change as a function of liquid thickness

In order to incorporate the numerous data curves presented in Fig.S3 into a compact numerical model which allows prediction of $h_c(t)$ under various driving optical powers, we fit the data to the following first order ordinary differential equation

$$\dot{h}_c(t) = \alpha(P)h_c(t) + \beta(P). \tag{S16}$$

Here, $h_c(t)$ is liquid thickness above gold patch center as a function of time t, P is a constant value of optical power carried by the WG, and the fit to simulation data is given

9

in Fig.S5a, and $\alpha(P)$ and $\beta(P)$ are power dependent coefficients explicitly given by

$$\alpha(P) = 0.4368 \cdot P - 0.0589; \quad \beta(P) = -0.5546 \cdot P + 0.0469, \tag{S17}$$

and are presented in Fig.S5b. It is worth mentioning that based on a fitting presented in Fig.S5a, a cubic fit would lead to additional terms in Eq.S16 but to small improvement in the model. We then employ Eq.S17 to predict liquid evolution $h_c(t)$ under power levels P and $2P$ (corresponding to logical 'zero' and 'one') during time window τ_w, and zero power during τ_r. Note that here P stands for the value of the optical power above the WG and not the power in the original input WG; the first coupler divides the power according to $2:1$ ratio $(\tan^2(0.6155) = 1/2)$ to compensate for the approximate 3 db loss due to Joule heating in the gold patch in the liquid cell. Consequently, the ratio of input power to the WG power is $3:2$. For each value of h_c we then employ the one-to-one relation between liquid thickness to corresponding phase change which is described in Fig.S5c.
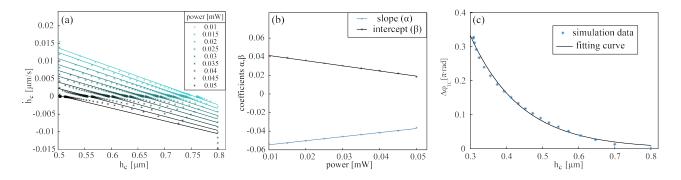

FIG. S5. (a) Linear fit evolution in the phase space $(\dot{h}, h)$ for different power values together with a linear fit given by Eq.S16. (b) Fitting of the coefficients α, β as a function of power. (c) The one-to-one relation between liquid thickness h_c above gold patch center and the self-induced phase change $\Delta\varphi_{TC}$. The fit (black curve) between the two quantities can be interpolated by $\Delta\varphi_{TC} = 2.786 \cdot \exp(-7.082 \cdot h)$.

S.5.3. Reservoir dynamics: fading memory and delayed 2-bit XOR

Consider evolution equation Eq.S16 with power dependent coefficients $\alpha(P), \beta(P)$ and assume that the power P maintains constant power levels on some time intervals (i.e. piecewise constant), similar to the behavior along $\tau_{W,r}$ intervals considered for XOR

task. Partition the total time period T into N arbitrary intervals at times $[t_0, t_1, ..., t_N]$ of corresponding lengths $[T_1, ..., T_N]$ where $t_N = T$, and furthermore assume that the liquid thickness at corresponding times is given by $[h_0, h_1, ..., h_N]$. For any interval where the optical power maintains constant value, the solution to Eq.S16 is given by

$$h(t) = -\frac{\beta}{\alpha} + \left(h_0 + \frac{\beta}{\alpha} \right) e^{\alpha t}, \tag{S18}$$

where h_0 is the initial thickness time ($t = 0$) and α, β are the corresponding values of the coefficients which are constant along the relevant time interval. Employing the solution given by Eq.S18 for each one of the intervals introduced by the partitioning above, yields

$$h_1 = a_0 + b_0 h_0; \quad a_0 = \frac{\beta_0}{\alpha_0} \left(e^{\alpha_0 T_0} - 1 \right); b_0 = e^{\alpha_0 T_0}$$

$$h_2 = a_1 + b_1 h_1 = a_1 + b_1 a_0 + b_1 b_0 h_0$$

$$...$$

$$h_n = a_{n-1} + b_{n-1} a_{n-2} + b_{n-1} b_{n-2} a_{n-3} + ... + b_{n-1}...b_1 a_0 + \underbrace{b_{n-1}...b_0 h_0}, \tag{S19}$$

where only the last term, highlighted by the curly bracket, depends on the initial thickness value h_0. Here, the constants a_k, b_k are defined by

$$a_k = \frac{\beta_k}{\alpha_k} \left(e^{\alpha_k T_k} - 1 \right); \quad b_k = e^{\alpha_k T_k}; \quad k = (0, ..., n-1), \tag{S20}$$

where α_k, β_k are the values of α_P and β_P, respectively, along the time interval T_k. Importantly, the last term h_0 is multiplied by a series of n numbers; each number b_k ($k = (0, ..., n-1)$) is smaller than unity because $\alpha(P) < 0$. Consequently, for sufficiently large number of steps n the last term will become arbitrary close to zero and therefore negligible compared to a_{n-1} and other terms. Fig.S6a presents the fading memory effect where the evolving thin liquid film, governed by Eq.S16, indeed 'forgets' the initial conditions as we derived in Eq.S19, and all curves approach towards a common attractor state. Fig.S6b presents test results of 2-bit XOR with delay $d = 2$ as a function of power and rest time (τ_r); as expected it admits lower accuracy compared to the $d = 1$ case presented in Fig.5. Furthermore, Fig.S6c presents test error of 2-bit XOR as a function of delay (d) for fixed power parameters thus illustrating that $d = 1$ can achieve minimal error and that generally other values of d lead to low accuracy.
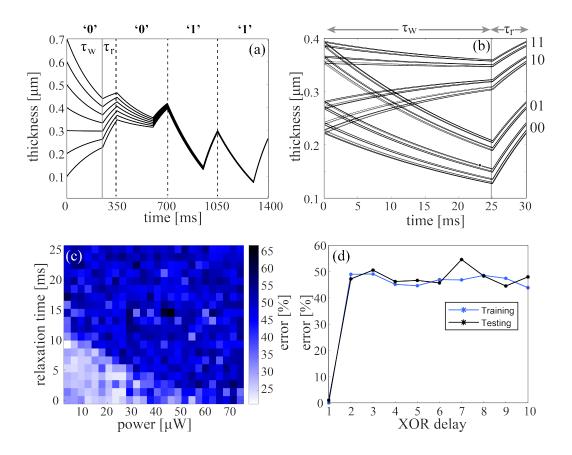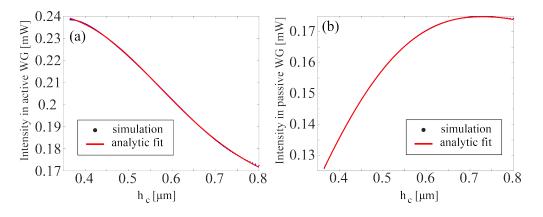
11

FIG. S6. Numerical results presenting: (a) illustration of the fading memory effect, where the evolving system 'forgets' the different initial conditions leading to convergence towards a common attractor state; (b) folded thickness dynamics diagram where thickness evolution in nonlocal circuit is divided to time intervals of length $T = \tau_w + \tau_r$ and plotted on top for each other between times $5T$ to $200T$. The diagram shows four main curves demonstrating four different combinations due to two possible actuation pulses and one step back in time dominant memory (key parameters: $\tau_w = 25$ ms, $\tau_r = 5$ ms, $P = 0.033$ mW); (c) test results of XOR gate with delay $d = 2$ ($\tau_w = 25$ ms, $\tau_r = 10$ ms). (d) Error performance of XOR operation as a function of delay d for the following parameters: $\tau_r = 10$ ms, $\tau_w = 25$ ms, $P = 0.06$ mW.

S.5.4. Nonlocal RC: relation between liquid thickness to the output light intensity

In this section we consider linear coupler geometry where the coupling region is covered with liquid. The heating in the gold patch in active WG leads to thickness change, which in turn modifies the coupling coefficient and the intensity in the output ports. Fig.S7a presents the corresponding geometry whereas Fig.S7b,c present intensity

12

in the active and passive WGs, respectively. The simulation points is fitted against a

FIG. S7. Multiphysics simulation result describing dependence of optical output power in active (a) as well as (b) passive WGs in a directional coupler geometry as a function of liquid film thickness, where the two parallel WGs have separation distance 500 nm (see Fig.5a). The analytic fit, given by Eq.S21, allows to employ this result in RC simulation.

simple analytical curve, given by

$$
\begin{aligned}
\text{active WG} &= (0.175 \cdot h_c^2 - 0.197 \cdot h_c + 0.088)/(h_c^2 - 0.978 \cdot h_c + 0.386) \\
\text{passive WG} &= (0.093 \cdot h_c^2 + 0.005 \cdot h_c + 0.014)/(h_c^2 - 0.66 \cdot h_c + 0.326),
\end{aligned}
\tag{S21}
$$

Eq.S21 thus allowing simpler implementation of nonlocal RC.

S.5.5. Comparison against optical-based and liquid-based RC platforms

In the following Table S2 we compare our Optofluidic concept with thin liquid film, against several other integrated chip-scale photonics approaches which include Phase change approach which relies on phase change transition, All-photonic approach which relies on optical delay without material response, as well as other modalities which rely on external modulation/feedback due to Electro-optic and Thermo-optic effects. For completeness we also provide Fluid-mechanical approach without optical interaction, which employs mechanical actuation of surface waves in liquid and their reflection from the large container boundaries as an internal feedback which can be employed for RC/NC computation.

Among the different criteria used to conduct the comparison we choose the magnitude of the corresponding refractive index change; if the feedback was realized by external

unit, delay or was it induced by internal nonlinear material response; size of the active area where the material response triggers induced nonlinear changes of the refractive index; energy per bit. Here, the Optofluidic approach presents the highest

	Index change	Area	Feedback	Time scale	Non-linearity	Non-locality	Energy per bit	Ref
Electro-optic	$O(10^{-4})$	$10 \times 10~\mu m^2$	external	$O(100~ps)$	×	×	500 fJ	[45]
Thermo-optic	$O(10^{-3})$	$4 \times 5~\mu m^2$	external	$O(100~\mu s)$	×	×	0.4 nJ	here
All-photonic	-	16 mm^2	delay	$O(300~ps)$	×	×	0.1 fJ	[14]
Phase change	$O(10^{-2})$	$0.4 \times 0.4~\mu m^2$	**internal**	$O(100~ns)$	✓	×	400 pJ	[47]
Fluid-mechanical	-	1×1 m^2	**internal**	$O(10~s)$	-	-	0.3 J	[43]
Optofluidic	$O(10^{-1})$	$0.5 \times 0.5~\mu m^2$	**internal**	$O(10~ms)$	✓	✓	10 nJ	here

TABLE S2. Comparison between several approaches capable in-principle to realize NC/RC tasks using integrated photonics chip-scale platforms, with internal and external feedback as main criteria which strongly affects the footprint of the photonic device. Electro-optic and Thermo-optic based approaches allow relatively efficient signal modulation of on-chip component in terms of energy (Electro-optic also in time), but require external control unit and hence additional space/energy resources. Phase change and Optofluidic approaches admit internal feedback due to matter response in a compact region, which results in a smaller footprint without optical feedback lines, yet these are not as fast as Electro-optic. All-photonic approach admits built-in photonic delay lines and requires very small operation energy, yet photonic delay lines translate into larger footprint compared to other chip-scale approaches. The energy per-bit in all cases is computed without considering the power needed to operate the corresponding detection system, and in Electro-optic and Thermo-optic approaches it also does not take into account the circulating optical energy in the circuit, which is lower compared to the corresponding values required to modulate the device. The macroscopic Fluid-mechanical approach is brought here for reference; it admits internal feedback due to reflection of water waves from container's boundaries, yet the macroscopic size of the mechanical actuators leads to meter sized system with much higher energy consumption.

index change due to the large refractive index contrast between gas and liquid media,

which presumably leads to high signal modulation and to higher performance of the corresponding NC/RC tasks. Importantly, while the Electro-optic and Thermo-optic approaches, require memorizing previous measurement results in external memory unit and introducing external feedback into the photonic circuit through electrical modulation of micro-ring resonator and metal heater in MZI device (shortly discussed below), respectively, Optofluidic and Phase-change approaches rely on internal feedback due to nonlinear material response and transient evolution of the excited state towards equilibrium which is employed as a memory at the same spatial location. For instance, in the Optofluidic approach the optically triggered liquid response allows to modulate the signal and also to serve as an optical memory without the need to introduce dedicated electrical/optical feedback loops. The corresponding energy per bit for the digital XOR task is given by 10 μW $\times$ 1 ms $=$ 10 nJ/bit (where 10 textμW is the energy allowing to support high performance as read from diagram Fig.5e), which is used for both optical transmission and actuation of nonlinear liquid response. Analogously, assuming MZI geometry similar to Fig.5a but with a metal heater approximately two microns above the WG, can lead to an optical phase shift if the temperature in the heater is externally modulated. In particular, assuming WG temperature increase is 20° which requires metal patch increase $\Delta T = 40^o$ degrees in order to achieve $\pi/2$ phase shift (see for instance for Applied Nanotools foundry test results https://www.appliednt.com/nanosoi/sys/resources/examples/tri-layer/), implies that the total heat energy is given by $q = \rho \cdot V \cdot c \cdot \Delta T \approx 7.5$ nJ. Here, we assumed parameters corresponding to integrated titanium-tungsten (TiW) heaters with density $\rho = 4429$ kg/m^3, specific heat $c = 526.3$ J/(kg $\cdot$ K), and volume $V = 0.2 \cdot 4 \cdot 100 = 80$ μm^3 of the 100 μm long metal patch. To achieve smaller modulation by a factor of 20, comparable to modulation of Optofluidic circuit presented in Fig.S7 which is sufficient for XOR implementation, requires shorter metal patch of length 100μm/20 $= 5$ μm and correspondingly smaller modulation energy $7.5/20 \approx 0.3$ nJ. The All-photonic approach on the other hand, presents an example of chip-scale system which enables to obtain a linear response (in electric field) due to delay lines which provide the capability to form interference between signals injected at different times, but it does not have built-in nonlinear matter response apart the square law detection. While in Phase change and Optofluidic modalities the nonlinearity stems from light-matter interaction between

WG modes to phase change substance or liquid, in the Fluid-mechanical approach the nonlinearity stems from inherently nonlinear evolution of the gas-liquid interface; linear evolution occurs in a small amplitude regime. Interestingly, while optical nonlinearity in the phase change approach is limited to a single WG, Optofluidic approach is the only one which allows to harness nonlocality for computation and even demonstrates superior performance compared to nonlinear effect (see Fig.5,6).

S.5.6. Analog task: row by row data injection

In Fig.6 we presented performance of nonlinear and nonlocal circuits, schematically presented in Fig.5(a,c), respectively, to perform the analog task of handwritten 'zero'/'one' classification based on 'bit-after-bit' parallel injection in two input arms, where the signal of each bit is proportional to the brightness value of the corresponding pixel in the image. Here, we present how the classification performance changes if one
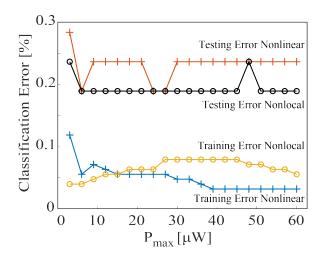

FIG. S8. Handwritten 'zero'/'one' classification based on parallel columns injection into nonlinear and nonlocal circuits. The two sets of curves marked with plus and circle correspond to performance of nonlinear and nonlocal circuits, respectively.

simultaneously injects a pair of columns instead of rows. Fig.S8 presents simulation results where the nonlinear and nonlocal circuits perform classification of handwritten 'zero'/'one' digits by employing parallel 'bit-after-bit' injection of two pairs of columns (28 bits long each); one column is injected in each one of the two input arms, similarly to the row injection scheme. We see that overall the performance is comparable to rows

16

injection presented in Fig.6, indicating that the degree of correlation generated between adjacent rows/columns is similar in the type of basic circuits we considered. While optimizing the injection scheme and constructing optimized task-dependent circuits is an important question, it is beyond the scope of this work.

S.5.7. Optofluidic RNN

While the circuits presented in Fig.5 employ single or two input WGs, it should require substantial computation time for task which admit large number of bits, including 'zero'/'one' handwritten classification task presented above. To achieve time-division multiplexing one can naturally employ more input waveguides each carrying independent information. Here, we present a basic example towards this
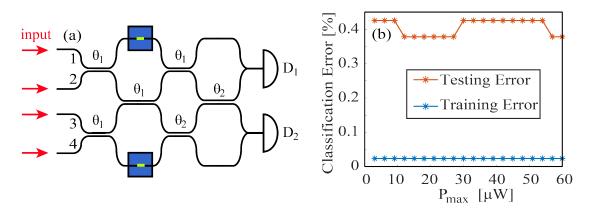

FIG. S9. Optofluidic RNN with internal feedback processing handwritten 'zero'/'one' classification. (a) Schematic representation of the network with four inputs and two liquid cells, and (b) the corresponding training and test results presenting the corresponding classification error.

direction by employing four inputs which decrease the computation time by a factor of two compared to the schemes presented in Fig.5(a,c). Fig.S9 presents an optofluidic network comprised of four inputs, pair liquid cells, six linear couplers (with coupling coefficients $\theta_{1,2}$), and a pair of optical detectors $D_{1,2}$.

Each input WG in scheme Fig.S9a, labeled as $1, 2, 3, 4$ receives a different line in the image according to $(4i - 3, 4i - 2, 4i - 1, 4i)$ where the $1^{st}/2^{nd}/3^{rd}/4^{th}$ entry in this vector corresponds to the input fed into WG $1, 2, 3, 4$, respectively, and $i = (1, .., N/4)$ where

$N = 28$ is the total number of rows in the image. Fig.S9b presents training and test error of 'zero'/'one' classification with similar performance compared to single MZI optofluidic circuit results presented in Fig.6, but allowing twice faster computation. Also, since the area of significantly deformed gas-liquid interface around the gold patch can be limited to only few microns or less (e.g. if the actuation does not operate for a long time), in principle larger number of WGs can be accommodated within a single liquid cell if cross talk nonlocal effects are not desired.

S.5.8. Preparatory experiments: liquid deposition and plausibility of the approach

To demonstrate feasibility of our approach from experimental point of view, especially controlling liquid deposition on a micron scale, we fabricated trenches in silicone chip and then deposited silicone oil into it. Reactive-ion etching (RIE) was used to etch the silicon WG, RIE and Buffered oxide etch (BOE) were used to remove the cladding silicon dioxide till buffer silicon dioxide layer without damaging the WG. Fig.S10a, which was generated by using Profilm 3D® (Filmetrics, San Diego, CA, USA), presents 3D silicone oil profile within square-shaped 50 μm cell wide and 3 μm deep, where the refractive index of silicone oil has the same refractive index as silicon dioxide in visible wavelength, so the 3D profile of the tranche filled with liquid could be generated by white light interferometry (WLI) method. Fig.S10b presents the profile of the gas-liquid interface along the diagonal AB. Fig.S10(c-e) presents top view microscopy image of the 50 μm cell hosting a WG (central horizontal line) and deposited liquid at three different stages: (c) empty, (d) partially filled, (e) fully filled. Note that due to wetting of the vertical walls, liquid thickness is thinner at the center reaching to sub micron thickness which according to our model is enough to initiate self-induced film deformation.

Note that in our modeling (e.g. Fig.2) we assumed initially flat gas-liquid interface, whereas in practice Fig.S10 presents curved interface with increasingly higher thickness as liquid film approaches 3 μm high vertical walls, and thin liquid film of minimal thickness ~ 200 nm in the central region above the WG. Nevertheless, the average slope of the interface is only $\sim (3 - 0.2)/25 \approx 0.11$ (where 25 μm denotes the minimal distance from cell's center to its boundary), and the WG is located at region where the liquid film has a minima point and hence the local slope is even smaller.

18

Our previous experiments where thin liquid film was deposited on gold plasmonic grating [25], indicates that thin liquid thinning can be invoked by external light illumination across a wide range of power levels. For instance ~ 400 mW can initiate large deformation which lead to liquid depletion (holes), whereas ~ 6 μW leads to subnanometer thickness changes. Importantly, in all cases the liquid film restored to initial configuration under surface tension forces. Since our modeling predicts that power levels of just around 0.1 mW (see Fig.2) are enough in order to achieve sufficiently high temperature increase and liquid deformation due to higher power density in the channel WGs, we believe that the proposed approach is promising in terms of future experimental realization.
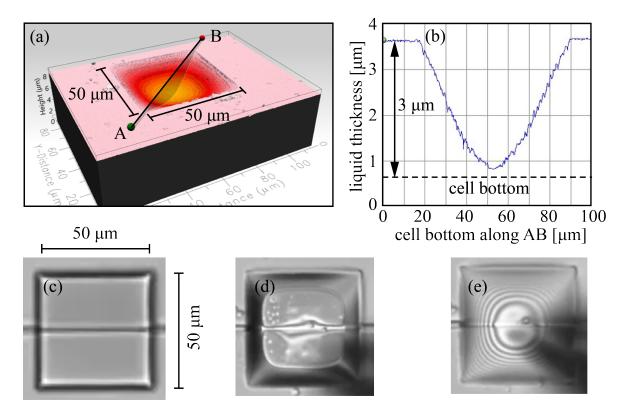

FIG. S10. Experimental images of silicone oil deposited into an etched $50 \times 50 \times 3$ μm^3 cell in buried oxide (BOX) layer. (a) 3D images presenting smooth oil surface, (b) oil film thickness along the diagonal AB, (c-e) top view presenting empty, partially filled, and full cell, respectively. The central horizontal line is a 500 nm wide silicon WG, which does not interfere with the process of controlled liquid deposition.

S.5.9. Self-induced absorption in the metal patch and the waveguide

Here, we investigate the effect of the gold patch on transmittance of the photonic modes as a function of mode's wavelength. Fig.S11 presents multiphysics simulation results of transmittance as a function of wavelength and of time in the spectral region between 1530 nm to 1580 nm, due to CW TM mode of power 0.07 mW, where Fig.S11a corresponds to the case of active WG described in Fig.2 whereas Fig.S11b corresponds to the case of active and passive WGs described in Fig.3. In particular, Fig.S11a describes the case of time dependent transmittance spectra where $t = 0$ ms corresponds to initially flat liquid film, whereas progressively later time moments with more prominent liquid deformation reveal emergence of transmittance dip around 1553 nm at $t = 40$ ms indicating higher quality factor and resonant absorption.
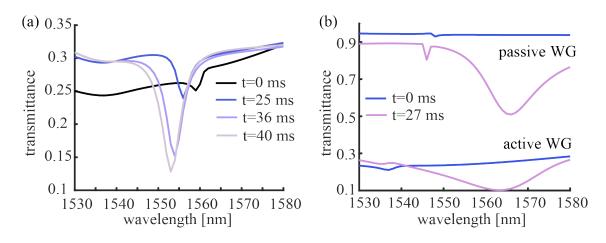

FIG. S11. Multiphysics simulation results presenting transmittance as a function of wavelength for different moments of time under CW 0.07 mW TM mode. (a) Single active WG described by Fig.2, (b) passive WG described by Fig.3. Note that for the passive WG at our working wavelength 1550 nm, only ~ 0.25 dB loss is induced by the gold patch and deformation of the thin liquid film.